Tellus (1987), *39A*, 354–375

The effect of vertical and slantwise convection on the simulation of polar lows

By THOR ERIK NORDENG, *Norwegian Meteorological Institute, P.O. Box 320-Blindern, N-0314 Oslo 3, Norway*

(Manuscript received 24 June 1986; in final form 13 January 1987)

ABSTRACT

Two polar low cases during February 1984 are simulated with a mesoscale limited area grid point model. The role of released latent heat on different scales as a driving mechanism for polar lows is investigated by studying a series of prognoses with condensation schemes for the large-, meso-, and cloud-scales. For the mesoscales, a parameterization method for slantwise convection is developed and applied. The simulations show that release of latent heat from condensation is crucial in order to obtain sufficiently strong developments. When working alone, large-scale condensation leads to unstable lapse rates and to fast developments. Convection shifts the area of maximum heating upwards and stabilizes the atmosphere, while slantwise convection in addition spreads the heating horizontally away from the surface disturbance. The large-scale response to parameterized slantwise convection is to stabilize the model atmosphere with respect to symmetric instability, to shift areas of ascending motion towards sloping absolute momentum surfaces and to enhance low-level winds.

1. Introduction

Polar lows are small-scale, intense vortices which develop in cold air north of the polar front. Their origin is of some uncertainty. Harrold and Browning (1969) suggested that they are caused by baroclinic effects. Rasmussen has in several papers (e.g., Rasmussen, 1981) proposed that polar lows forming in the Atlantic Ocean are CISK driven. CISK (Conditional Instability of the Second Kind) is a self exciting system where convective condensation becomes sufficiently organized to have a positive feedback between the cloud scale and the developing vortex scale. Bratseth (1985) has shown analytically that the CISK mechanism is strong enough for polar lows to develop on a short time scale. A necessary condition for this is that the latent heat is released at low levels. The oceanic heat flux plays an important role for the development of polar lows as shown by Økland (1977). Other investigators (e.g., Reed, 1979; Sardie and Warner, 1983, 1985) conclude that polar lows develop from a combination of baroclinic instability release and the CISK mechanism.

The question about the origin of polar lows is of more than academic interest. In order to forecast the development and life-cycle of polar lows numerically, one has to bear in mind that the governing equations of motion nicely reproduce baroclinic processes on a scale of practical use in numerical weather prediction models. If release of potential energy through baroclinic processes is the main driving mechanism of polar lows, the problem of numerically forecasting them reduces to an initial value problem. (This is of course a substantial problem on its own but will not be discussed here.) The CISK mechanism is, however, a positive feedback between organized convection on the cloud scale and the scale of the growing vortex. The cloud scale is not resolvable in numerical models and the modeller then runs into the problem of parameterization. Such a parameterization may be very intricate since the CISK mechanism is not completely understood.

Most attention has been paid to convection in barotropic environments, the knowledge about the baroclinic counterpart is less. By assuming thermal wind balance in the along front direction, Eliassen (1962) derived a diagnostic equation describing the transverse (sloping) ageostrophic circulation in frontal zones (Eliassen-Sawyer equation). The forcing terms of the equation are geostrophic confluence and/or shear and diabatic processes. Potential vorticity plays the role as a stability parameter. The equation becomes hyperbolic for negative potential vorticity, suggesting strong convective motion in the most unstable direction. Conditional symmetric instability (Bennets and Hoskins, 1979) and wave-CISK (Emanuel, 1982) have been suggested to be responsible for rainbands near fronts. Emanuel (1983b) showed an example of an apparent slanted convection where the atmosphere was conditionally stable for vertical convection, but unstable for convection along a surface of constant absolute momentum. Seltzer, Passarelli and Emanuel (1985) address the need for a parameterization scheme for heat and momentum transport due to symmetric instability in numerical models. Thorpe and Nash (1984) incorporated parameterization of vertical convection into the diagnostic Eliassen-Sawyer equation to see the effect of various closure assumptions and heating distributions. In Thorpe (1984) this work was extended to take into account convection along an absolute momentum surface. Recently, Thorpe (1986) has proposed a scheme to parameterize slantwise convection based upon an adjustment towards a stable stratification. Here, an independently developed scheme for the parameterization is given and applied on real data in a three dimensional numerical weather prediction model. Conditions favourable for slantwise convection are low static stability and strong thermal wind. These conditions are frequently met in connection with polar lows, and slantwise convection may be one key in the understanding of the developing mechanism of polar lows.

Some numerical simulations of polar lows exist in the literature. Sardie and Warner (1985) simulated the life cycles of two polar lows numerically (one Atlantic and one Pacific case) with emphasis on the role of diabatic processes. They showed that a correct parameterization of condensation is essential. In fact, it was necessary to include a convective parameterization to prevent overdevelopment for one of their cases. Grønås, Foss and Lystad (1987) simulated 6 polar low cases with a 50 km resolution meso-scale model, including the two cases studied here. It turned out that the model was able to correctly modify the large-scale initial fields according to the mesoscale forcing and resolution. It forecasted the surface disturbances at approximately the correct time and place, but the final rapid and strong growth of the deepening vortices on a short time scale were too weak. One of their test cases was run with a 25 km resolution model (in fact the case of 27 February 1984 studied here), with improved results compared to the 50 km reference experiment (Grønås et al., 1987).

This investigation is a follow up of their experiments. The role of condensation processes in the development of polar lows is emphasized by numerical simulations of two of the polar low cases studied by Grønås et al. (1987). Condensation schemes for large-, meso-, and cloud-scale condensation processes are developed and applied. The mesoscale condensation scheme is a novel parameterization of slantwise convection. The cloudscale condensation scheme treats deep convection. One aim of the paper is to see the effect of condensation schemes on different scales. Accordingly, the condensation schemes are simple, but consistent with respect to each other. Tests among schemes within a certain scale (for instance between different schemes for deep convection) are omitted.

The model and physical parameterization are documented in Section 2. A detailed description of the scheme for representing slantwise convection including a discussion of the applicability of using the scheme for curved flow, is given in Section 3. The polar low cases and numerical experiments are described in Section 4. Section 5 pays attention to the effect of condensation on different scales, including the results obtained with the new scheme. Section 6 contains discussions. In Appendix the Slantwise Convective Available Potential Energy (SCAPE) as defined by Emanuel (1983b) is related to the method used here.

2. The model and physical parameterization

The model used is the operational mesoscale model at the Norwegian Meteorological Institute (Grønås and Hellevik, 1982; Grønås et al., 1987). The vertical coordinate is $\sigma = (p - p_t)/(p_s - p_t)$, where p_s is surface pressure and p_t is 200 mb. The model is run with 10 layers defined by the 11 σ-surfaces (0.0, 0.1875, 0.375, 0.525, 0.675, 0.750, 0.800, 0.850, 0.900, 0.950, 1.00). The horizontal resolution is 50 km. The orography is interpolated from hand-read terrain elevation (resolution 0.5° latitude, 1° longitude). At lateral boundaries the model variables are relaxed towards given large-scale variables. Surface fluxes of heat, moisture and momentum are based on Monin-Obhukov similarity theory. In the free atmosphere, vertical diffusion is parameterized by a simple first-order closure scheme. The exchange coefficients depend on the local Richardson number. Sea surface temperatures are climatological. Since this version of the model does not compute ground surface temperature explicitly, we do not allow surface fluxes of heat and moisture over the marginal land-areas within the integration domain. Since the land is snow covered, the PBL in these areas is usually very stable. This simplification of the model is not believed to influence the results significantly. References are made to Grønås et al. (1987) for a detailed description of the model.

2.1. *Large scale condensation*

Large-scale condensation (also called non-convective condensation) is based upon removal of supersaturation with the released latent heat warming the air. The scheme is diagnostic. The model equations are first integrated one step forward without condensation processes included. These effects are added in a second step. The scheme is used if supersaturation is found at a grid point. The excess moisture is condensed with the latent heat warming the air such that the air is exactly saturated after the moisture has condensed. The implicit equations to be solved are:

$$q + \delta q = q_{\text{sat}}(T + \delta T), \tag{1a}$$

$$c_p \delta T + L \delta q = 0, \tag{1b}$$

where δq and δT are changes in specific humidity and temperature to be found, q the preliminary specific humidity, T the preliminary absolute temperature, and q_{sat} is specific humidity at saturation. Here, as well as in the rest of this paper, notation is conventional except when stated. (1a) expresses that the air after adjustment shall be exactly saturated, while (1b) secures that the enthalpy of the air is conserved. The right-hand-side of (1a) may be expanded in a Taylor-series. By retaining the first order term and utilizing the Clausuis-Clapeyron equation, one obtains:

$$\delta q = \frac{q_{\text{sat}}(T) - q}{1 + \dfrac{\varepsilon L^2 q_{\text{sat}}(T)}{c_p R T^2}}, \quad \delta T = -\frac{L}{c_p} \delta q.$$

Precipitation is computed from,

$$R = \int_p \delta q \frac{dp}{g},$$

i.e., the sum of contributions from each grid point in a vertical column. It is assumed that there is an instantaneous release of precipitation. There is no evaporation of raindrops.

2.2. *Vertical convection*

If an air parcel becomes saturated in a conditionally unstable atmosphere, convection may take place. The problem of how an air parcel might enter a conditionally unstable region is discussed below, here it is assumed that by some kind of forcing the air parcel is lifted to the level of free convection from where it starts a buoyant ascent. Using the "top hat assumption", the vertical grid column is divided into a cloudy part (fraction a) and a cloudfree part (fraction $1 - a$) so that the preliminary integrated temperature and moisture (q, T) is redistributed into cloudy (index c) and cloudfree variables (index g) under the constraint that the integrated enthalpy is conserved.

$$\int_{\text{top}}^{\text{lift}} (Lq + c_p T)\, dp = \int_{\text{top}}^{\text{base}} a((Lq_c + c_p T_c) + (1 - a)(Lq_g + c_p T_g))\, dp + \int_{\text{base}}^{\text{lift}} (Lq_b + c_p T_b)\, dp. \tag{2}$$

"Top" means cloud top, "base" cloud base, "lift" is the level of parcel origin, and index b means a PBL (Planetary Boundary Layer) value. In the classical Kuo-scheme (Kuo, 1965), a is taken as a constant within the cloud and $q_g = q$, $T_g = T$, and $T_b = T$. a may then be computed from:

$$a = \int_{\text{base}}^{\text{lift}} (q - q_b)\,\mathrm{d}p \Big/ \int_{\text{top}}^{\text{base}} (q_c - q + c_p L^{-1}(T_c - T))\,\mathrm{d}p. \tag{3}$$

Remembering that a is the area covered by the convective system, adjusted values of q and T are, respectively:

$$\begin{aligned} q' &= aq_c + (1 - a)q, \\ T' &= aT_c + (1 - a)T. \end{aligned} \tag{4}$$

Heating, moistening, and precipitation are then given by

$$\begin{aligned} \delta T &= a(T_c - T), \\ \delta q &= a(q_c - q), \\ \delta R &= c_p \delta T \Delta p/(gL). \end{aligned} \tag{5}$$

To close the scheme, "the cloud" (T_c, q_c) and the numerator $\int q - q_b \mathrm{d}p$ have to be specified. This point will be considered below.

Most existing convection schemes are constructed to work in connection with tropical cyclones or in the tropics in general where deep convection is an extremely important physical process in the atmosphere. But it is not *a priori* certain that these schemes work well for middle and high latitudes. The kind of scheme described here is of the Kuo-type (Kuo, 1965, 1974). This widely used scheme assumes that cumulus convection occurs in regions of deep layers of conditionally unstable stratification and mean low level convergence. According to this hypothesis, the numerator in (3) is taken as the net moisture convergence including surface fluxes into a grid column during the time $\mathrm{d}t$, $(q - q_b = -(\nabla \cdot q\boldsymbol{v})\,\mathrm{d}t)$. This relation may be derived formally by relating heating in saturated updraughts to individual changes of specific humidity $(Q = -L\,\mathrm{d}q/\mathrm{d}t)$ with the assumption that the *local* change of specific humidity $(\partial q/\partial t)$ vanishes. Kuo and Anthes (1984) discuss several aspects of this kind of convection closure. For midlatitude convective systems it is important that a fraction of the converged moisture goes into a general moistening of the grid-column (Kuo and Anthes, 1984). This is probably even more important at high latitudes where cold arctic air may change substantially by heating and moistening from the open sea. Kuo and Anthes (1984) showed in a case study that there is a strong correlation between large scale moisture convergence and precipitation rate. However, there is a time lag of several hours between the moisture convergence and the rainfall, indicating that a general moistening is important in the first phases of a convective storm, while most of the converged moisture is condensed in the mature phase of the storm. Since no really satisfactory theory of how to determine the fraction of the converged moisture to be used for a general moistening exists, the problem is circumvented by allowing the model equations to create a moisture profile without interference from the convection scheme. From the lowest layer within the unstable PBL (lift), air is lifted along a dry adiabat to the lifting condensation level (base). Within the unstable PBL, the specific humidity is assumed to be constant. A representative value of q_b is taken as the value obtained at the PBL top when all processes other than convection have been at work. A cloud profile of T_c and q_c is found by

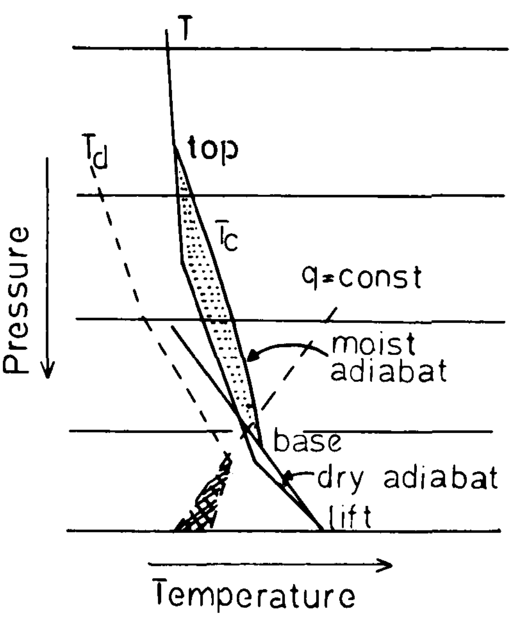

Fig. 1. Schematic diagram of how vertical convection may be initiated. The dotted area represent CAPE (Convective Available Potential Energy), while the doubled hatched areas represent available moisture for convection.

following a moist adiabat from the lifting condensation level (base) until the buoyancy becomes negative (top). The process is illustrated in Fig. 1.

Physically, this may be viewed upon as a simple parameterization of a (deep) convective boundary layer. The scheme used for time integration of vertical diffusion is conditionally stable. In practice, this means that the largest possible exchange coefficients are those obtained for neutral stratifications. For unstable conditions (free convective limit), the mixing length should approach height ($1 \sim z$). In some diffusion schemes (e.g., in the ECMWF-model; Louis, 1979) this is incorporated into the formulation defining the exchange coefficients. In nature, convective cells efficiently mix the boundary layer, but turbulent eddies on smaller scales are still present. Here, the latter effect is taken care of by the vertical diffusion scheme, while the former is parameterized by the above mentioned method. It should be remarked that the method only works when the boundary layer is coupled to deep convection. Treatment of a bounded convective boundary layer is probably poor.

3. Slantwise convection

As geostrophic deformation tends to increase horizontal temperature gradients, a cross-frontal ageostrophic circulation is set up to restore thermal wind balance. In this kind of motion potential vorticity plays the same role as static stability for vertical motion (Eliassen, 1962). The necessity of positive potential vorticity is more general than applied to this kind of two-dimensional motion. In Iversen and Nordeng (1984) it was shown that potential vorticity must be positive in order to have an elliptic set of equations for the balanced model (Charney, 1962). In pressure coordinates, potential vorticity is given as

$$P = -g\left(\eta \frac{\partial \theta}{\partial p} - \boldsymbol{k} \cdot \nabla \theta \times \frac{\partial \boldsymbol{v}}{\partial p}\right) \tag{6}$$

where η is absolute vorticity ($\eta = v_x - u_y + f$). If phase changes of water can take place, equivalent potential temperature (θ_e) is conserved and moist potential vorticity is defined with the same equation except that θ is replaced by θ_e.

$$P_e = -g\left(\eta \frac{\partial \theta_e}{\partial p} - \boldsymbol{k} \cdot \nabla \theta_e \times \frac{\partial \boldsymbol{v}}{\partial p}\right). \tag{7}$$

The scheme for parameterization of symmetric instability/slantwise convection is based upon an adjustment towards positive potential vorticity whenever negative values are found. There are several ways this can be done. A reference sounding (θ_{ep}) to be adjusted towards may be derived from (7) assuming vanishing moist potential vorticity.

$$\partial \theta_{ep}/\partial p = \eta^{-1} \boldsymbol{k} \cdot \nabla \theta_e \times \partial \boldsymbol{v}/\partial p. \tag{8}$$

Assuming that the right-hand side of (8) may be computed from the model variables, the reference sounding is derived by integration through the unstable part of the model atmosphere (p_{lift} to p_{top}). θ_{ep} at lifting level is taken as θ_e at the lowest model level where negative potential vorticity is found. Thorpe (1986) proposed a scheme where θ_e is adjusted towards θ_{ep} within a time τ, i.e.,

$$(\partial \theta_e/\partial t)_{\text{adj}} = (\theta_{ep} - \theta_e)/\tau.$$

The time of adjustment (τ) must be chosen. Here it will be tried to go a bit further by taking the kind of flow we want to parameterize into consideration.

The stream function given by the Eliassen-Sawyer equation may cursorily be described as ellipses with their primary axis along an absolute momentum surface, ($M = fx + v$). x is the coordinate axis perpendicular to the frontal zone and v is the along front wind component. The equation becomes parabolic for vanishing potential vorticity suggesting strong (convective) motion following M-surfaces. The actual unstable motion (for negative potential vorticity) follows potential temperature surfaces. The difference between θ_e-surfaces and the absolute momentum surfaces are usually small and even the unstable motion may be considered to be along absolute momentum surfaces. Observations from frontal zones indicate that after a period of slantwise convection, θ_e tends to be mixed along absolute momentum surfaces (e.g., Emanuel, 1985), so that $(\partial \theta_e/\partial z)_M = 0$. The relation between this (moist adiabatic stratification *along* an M-surface) and vanishing potential vorticity is easily demonstrated by the coordinate transformation,

$$X = M = fx + v, \qquad Z = p, \tag{9}$$

which, for two-dimensional motion where v is the along front wind component and $\partial/\partial y = 0$), give,

$$(\partial/\partial Z)_M = \partial/\partial p - \eta^{-1}(\partial v/\partial p)(\partial/\partial x), \tag{10}$$

so that,

$$\eta(\theta_e/\partial Z)_M = \eta\,\partial\theta_e/\partial p - (\partial v/\partial p)(\partial\theta_e/\partial x)$$
$$= -g^{-1} P_e = 0, \tag{11}$$

i.e., instead of constructing a moist adiabat *along* an absolute momentum surface (M), one can compute the *vertical distribution* of θ_e which corresponds to moist adiabatic stratification along M. Emanuel (1983b) showed that potential energy for slantwise convection, SCAPE, is the positive area on a tephigram obtained when a parcel is lifted along a surface of constant absolute momentum and the temperature of the parcel (θ_p) is compared to that of the environments (θ).

$$\text{SCAPE} = g\overline{\theta^{-1}} \int_M (\theta_p - \theta)\,dz = -\int_M (\theta_p - \theta)\,d\pi. \tag{12}$$

π is the Exner function: $\pi = c_p(p/p_0)^{R/c_p}$. He also showed that SCAPE may be estimated from the vertical distribution of the model variables

$$\text{SCAPE} = \text{CAPE} + \int_{z_0}^{z_1} (f/2\eta)\frac{d}{dz}((v - v_0)^2)\,dz, \tag{13}$$

where CAPE (Convective Available Potential Energy) is the usual area measured for vertical lifting on a tephigram (area between the moist adiabat from the lifting condensation level and the actual sounding). The last term is the contribution from the thermal wind, which may be large enough to compensate for significant negative values of CAPE due to vertical wind shear (see Fig. 2). In the Appendix (13) is derived directly from (8) by use of the thermal wind relation. From experiments on slantwise convection with a diagnostic model on constructed data, Thorpe (1984) concludes that a CISK formulation where the heating from convection is proportional to the low level vertical velocity and to SCAPE and distributed along an absolute momentum surface, is more likely to represent heating due to mixing of θ_e along M-surfaces than for heating proportional to the local vertical velocity w.

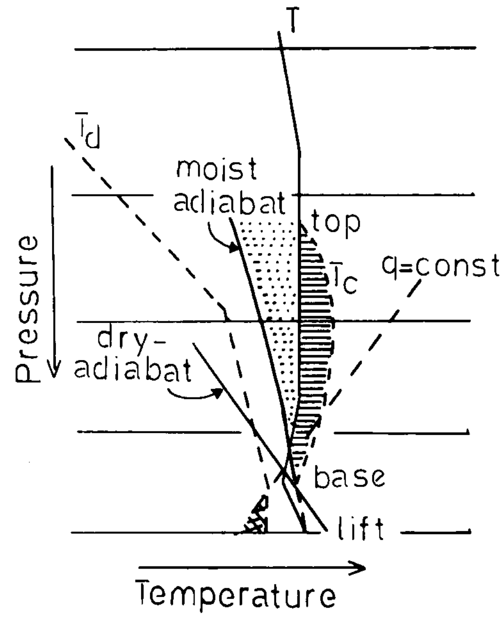

Fig. 2. Schematic diagram of how slantwise convection may be initiated. The horizontally hatched area represent SCAPE (Slantwise Convective Available Potential Energy), the dotted area represent CAPE, while the doubled hatched area represent available moisture for convection.

We are now able to design our parameterization scheme. Preferably it shall distribute heat along absolute momentum surfaces and the heating be proportional to SCAPE. As shown above, the difference in temperature between a parcel reversibly lifted along an absolute momentum surface and the environments may be computed from the difference between the modified cloud temperature obtained from vertical integration of (8) and the environmental temperature at the grid point. Temperature and specific humidity within the reference sounding are obtained by solving for temperature and specific humidity (T_c, q_c) from θ_{ep} by using the approximate equation defining equivalent potential temperature ($\theta_e = (c_p T + Lq)/\pi$). Below the condensation level (base), (T_c, q_c) is found from

$$\theta_{ep} = (c_p T_c + Lq_{lift})/\pi, \quad q_c = q_{lift}.$$

The reference (cloud) sounding is assumed to be saturated above the lifting condensation level,

$$\theta_{ep} = c_p T_c + Lq_{sat}(T_c)/\pi. \tag{14}$$

By the expansion,

$$q_{sat}(T_c) \simeq q_{sat}(T) + \frac{\varepsilon L q_{sat}(T)}{RT^2}(T_c - T), \tag{15}$$

one obtains,

$$T_c = T + \frac{\pi(\theta_{ep} - \theta_{es})}{c_p + \dfrac{\varepsilon L^2 q_{sat}(T)}{RT^2}}, \quad q_c = q_{sat}(T_c), \tag{16}$$

where θ_{es} is the equivalent potential temperature of a saturated environment, $(\theta_{es} = \theta + Lq_{sat}(T)/\pi)$. Cloud top is defined as the level where the buoyancy vanishes $(T_c < T)$. We may now proceed exactly as for vertical convection, but use the modified temperature (T_c) and specific humidity (q_c) in eq. (3) and (5). This procedure gives a *vertical distribution* of heating and moistening due to slantwise convection consistent with heating proportional to SCAPE, and determines the tendencies of T and q within the cloud. These tendencies are then interpolated on the actual absolute momentum surface.

The local surface of constant absolute momentum M may be written as

$$M = fs + V_n \tag{18}$$

where s is the horizontal distance along the direction $\boldsymbol{i}_s$,

$$\boldsymbol{i}_s = -\nabla\theta/|\nabla\theta|, \tag{19}$$

and V_n is the wind component normal to the direction $\boldsymbol{i}_s$:

$$V_n = \boldsymbol{v}\cdot\boldsymbol{k} \times \boldsymbol{i}_s. \tag{20}$$

The horizontal distance s from the grid point to the point where the M-surface crosses the level π is found from

$$fs(\pi) + V_n(\pi, s) = f\cdot 0 + V_n(\pi_0, 0),$$

which is equivalent to

$$s(\pi) = f^{-1}(V_n(\pi_0, 0) - V_n(\pi, s)) \tag{21}$$

or approximately,

$$s(\pi) = f^{-1}(V_n(\pi_0, 0) - V_n(\pi, 0)). \tag{22}$$

To summarize, a *vertical* distribution of δT and δq is derived from (3) and (5) using the modified cloud sounding as explained above. The *direction* for horizontal distribution of heating is given by $\boldsymbol{i}_s$, and the *distance* from the vertical axis to the point where the M-surface crosses a given level π is determined by (22). Coordinates relative to the grid point (i, j) are:

$$\mathrm{d}x = s\boldsymbol{i}_s\cdot\boldsymbol{i} = -\frac{s\theta_x}{(\theta_x^2 + \theta_y^2)^{1/2}}h^{-1}, \tag{23}$$

$$\mathrm{d}y = s\boldsymbol{i}_s\cdot\boldsymbol{j} = -\frac{s\theta_y}{(\theta_x^2 + \theta_y^2)^{1/2}}h^{-1}, \tag{24}$$

where h is the grid length. The tendencies (δT and δq) are then distributed among the four grid points surrounding $(\mathrm{d}x, \mathrm{d}y)$ according to:

$$\begin{aligned}
\delta T_1 &= (1-\mathrm{d}x)(1-\mathrm{d}y)\,\delta T, & \delta q_1 &= (1-\mathrm{d}x)(1-\mathrm{d}y)\,\delta q\\
\delta T_2 &= \mathrm{d}x\,(1-\mathrm{d}y)\,\delta T, & \delta q_2 &= \mathrm{d}x\,(1-\mathrm{d}y)\,\delta q\\
\delta T_3 &= (1-\mathrm{d}x)\,\mathrm{d}y\,\delta T, & \delta q_3 &= (1-\mathrm{d}x)\,\mathrm{d}y\,\delta q\\
\delta T_4 &= \mathrm{d}x\,\mathrm{d}y\,\delta T, & \delta q_4 &= \mathrm{d}x\,\mathrm{d}y\,\delta q.
\end{aligned} \tag{25}$$

The method allows for a horizontal as well as vertical distribution of heating and moistening due to slantwise convection. This is demonstrated in Fig. 3.

When the atmosphere is unstable to vertical and slantwise convection at the same time, the most unstable direction is vertical (Emanuel, 1983b). The sounding is therefore checked for symmetric instability only if conditions for vertical convection are not fulfilled. The absolute momentum M may be regarded as a generalized angular momentum. Since air is redistributed along a constant M-surface, this means that the angular momentum transport is automatically taken care of. Accordingly, the scheme for slantwise convection is consistent with regard to momentum transport.

As seen, the schemes for both vertical and slantwise convection are based upon the original Kuo-assumption (Kuo, 1965) in that heating and moistening are proportional to cloud/environment-deficits of temperature and humidity. The Kuo-scheme has undergone several refinements since it was suggested more than twenty years ago (for instance by Kuo, 1974; Anthes, 1977; Krishnamurti et al., 1976; Molinari and Corsetti, 1985). In particular, the method for moistening the environments is changed substantially from the original Kuo assumption. The convective

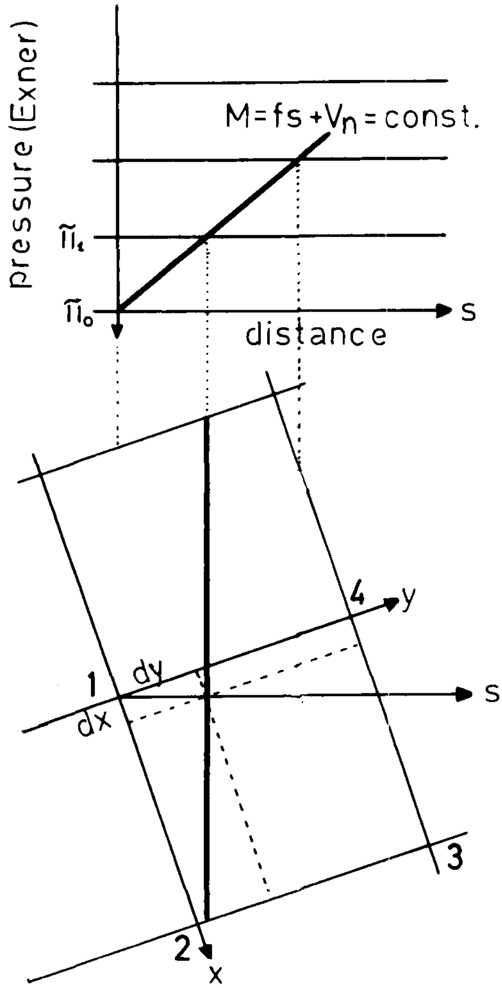

Fig. 3. Figure showing a possible geometric configuration for an absolute momentum surface M and the model grid. The upper part shows a vertical section along the temperature gradient (s increases downgradient). The M-surface is locally perpendicular to this direction and crosses a pressure surface (π_1) along the thick line in the lower part of the figure which is a horizontal section. Coordinates relative to the actual grid point for the intersection between the M-surface and the constant pressure surface (π_1) along the s-direction is shown in the lower part of the figure.

schemes studied here are chosen to be as simple as possible to focus on the difference between heating distributed vertically and along a sloping surface. In addition, the chosen methods make the convective schemes consistent with respect to each other.

3.1. Resolution and applicability to curved flow

The slope of the M-surfaces is given by the equation:

$$\left(\frac{\partial s}{\partial z}\right)_M = -\frac{\partial V}{\partial z}\bigg/\left(f+\frac{\partial V_n}{\partial s}\right), \tag{26}$$

and a horizontal length scale is given by

$$L = \frac{V_z D}{f+\dfrac{\partial V_n}{\partial s}},$$

where D is the vertical scale. Taking liberal estimates, ($D = 1$ km, $V_z = 10$ m s^{-1}/1 km, and $f+\partial V_n/\partial s = 10^{-4}$ s^{-1}), give $L = 100$ km. This kind of motion clearly belongs to the meso-scales, and a natural question is if it is necessary to parameterize it at all in a meso-scale model with resolution 50 km. One should then remember that a two grid-length signal is not resolved in a grid point model, so that phenomena of the order of the grid length and smaller have to be parameterized to be taken into account. There is, however, another length scale to be considered, the width of the convective updraughts. As shown from two-dimensional models (e.g., Thorpe, 1984; Thorpe and Emanuel, 1985; Emanuel, 1985) the updraught region becomes extremely narrow as the potential vorticity vanishes. This length scale is certainly not resolved by the present 50 km grid-point model.

The scheme is used in a general three dimensional model, and applied when the modified cloud sounding (16), shows an unstable stratification. Transformation to natural coordinates for an axisymmetric vortex reveals the applicability of the scheme for curved flow. In natural coordinates, moist potential vorticity is,

$$P_e = -g(\eta\,\partial\theta_e/\partial p - (\partial v/\partial p)(\partial\theta_e/\partial s)). \tag{27}$$

s is the radius and the wind is given by $\boldsymbol{v} = v\boldsymbol{k}\times\boldsymbol{i}_s$, where $\boldsymbol{i}_s$ is a unit vector pointing radially outwards. Absolute vorticity η is,

$$\eta = f + v/s + \partial v/\partial s. \tag{28}$$

Here, v/s is curvature vorticity, while $\partial v/\partial s$ is shear. For an axisymmetric vortex, angular momentum ($L = fs^2/2 + vs$) is conserved for non-viscous displacements, not absolute momentum

($M = fs + v$). The coordinate transformation, $X = L = fs^2/2 + vs$, $Z = p$, gives,

$$\eta(\partial\theta_e/\partial Z)_L = \eta\, \partial\theta_e/\partial p - (\partial v/\partial p)(\partial\theta_e/\partial s) = -P_e/g, \tag{29}$$

while the coordinate transformation $X = M = fs + v$, $Z = p$, gives,

$$\eta'(\partial\theta_e/\partial Z)_M = \eta'\, \partial\theta_e/\partial p - (\partial v/\partial p)(\partial\theta_e/\partial s)$$
$$= -P_e/g - (v/s)(\partial\theta_e/\partial p), \tag{30}$$

$$\eta' = \eta - v/s = f + \partial v/\partial s.$$

For vanishing potential vorticity ($P_e = 0$), this implies,

$$(\partial\theta_e/\partial Z)_M = -\frac{(v/s)(\partial\theta_e/\partial p)}{f + \partial v/\partial s}. \tag{31}$$

The "error" (31) vanishes for rectilinear frontal zones ($s \to \infty$), but increases for strong curvature (s small). Introducing $\partial\theta_e/\partial p$ from (29) and $\partial\theta_e/\partial s$ from the thermal wind relation for saturated air (A.4), give,

$$(\partial\theta_e/\partial Z)_M = -\frac{(v/s)(\partial v/\partial p)^2 f\rho\theta_e}{(f + \partial v/\partial s)\eta\gamma}, \tag{32}$$

where γ is the ratio between the moist adiabatic and dry adiabatic lapse rates. Taking liberal estimates, $(v/s) = \partial v/\partial s = f = 1.10^{-4}\ \mathrm{s^{-1}}$, $\rho = 1.2\ \mathrm{kg/m^3}$, $\theta_e = 300$ K, $\partial v/\partial p = 20\ \mathrm{m\,s^{-1}/200\ hPa}$, $\gamma = 0.5$, give,

$$(\partial\theta_e/\partial Z)_M = -1.2\ 10^{-4}\ \mathrm{K/Pa}.$$

Since $P_e = -g\eta\, \partial\theta_e/\partial Z$, this means that one adjusts towards a slightly stable rather than neutral stratification (for cyclonic vorticity).

4. The experiments

The model is used on two polar low cases from the winter of 1984. Both cases are run from ECMWF large-scale operational analyses. At the lateral boundaries ECMWF analyses are used for the 27. February case, while forecasts from the operational 150-km model of the Norwegian Meteorological Institute (Grønås and Hellevik, 1982) run from the same initial fields (ECMWF-analyses) are used for the 1 March case. Details about data preparation, interpolation to the model grid, and treatment of lateral boundary values are found in Grønås et al. (1987). They also studied the rôle of using prognoses versus analyses at lateral boundaries. The experiments are summarized in Table 1.

Table 1. *Experiments with different condensation schemes*

I	DRY	no heating of air due to condensation, no moisture cycle, surface heat flux and vertical diffusion of sensible heat present.
II	NOC	convective schemes turned off, heating and moistening due to large-scale condensation.
III	VC	large-scale condensation and vertical convection.
IV	SLVC1	large scale condensation, vertical convection and slantwise convection. heating and moistening due to slantwise convection are applied at the grid point.
V	SLVC2	same as (IV) but heating and moistening due to slantwise convection are interpolated onto the absolute momentum surface.

4.1. The cases

The low of 1 March 1984 develops on a southward-moving frontal zone in the Norwegian Sea. The zone consists of a tongue of warm air with colder air at both sides. Fig. 4 shows ECMWF operational analyses of 1000 hPa heights and temperature 12.00 GMT 29 February 1984. As the fronts move southward, strong surface winds and abrupt windshifts are observed. On 06.00 GMT 1 March 1984 the front passes the weather ship M (65.6°N, 2.5°E). Wind gusts up to 30 m/s are reported. The mature vortex as seen from satellite pictures develops at a later stage, but also the mesoscale frontal system classifies as a polar low event by the definition of Wilhelmsen (1985). Approximately 12 hours later (14.45 GMT 1 March 1984) a mature vortex is found in satellite pictures off the coast of Norway (Fig. 5). Nearby, at Vigra Airport (62.5°N, 6.1°E) wind gusts up to 33 m/s are reported and the airport is temporarily closed.

The 27 February case is the polar low from which the NOAA Arctic Cyclone Experiment made detailed three-dimensional observations

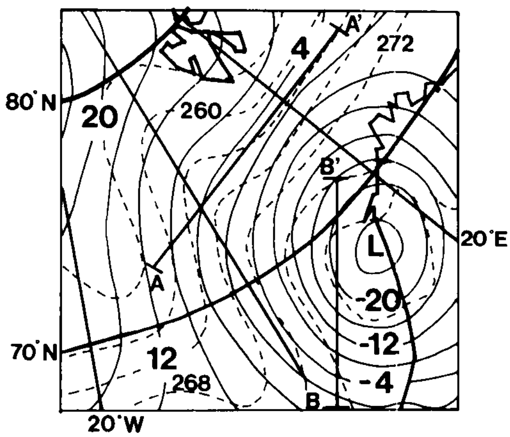

Fig. 4. Contours of 1000 hPa (solid lines, at intervals of 4 da m) and (potential) temperature at 1000 hPa (dashed lines at intervals of 4 K) for 12.00 GMT 29 February 1984. Heavy lines are cross sections for Fig. 7 (AA′) and for Fig. 8 (BB′).

(Shapiro et al., 1987). At 00.00 GMT 26 February 1984 there is a southwesterly flow across the Norwegian Sea. The cold air along the eastern coast of Greenland progresses southwards. Fig. 6 shows ECMWF analysis of 1000 hPa heights and temperature 00.00 GMT 26 February 1984. Within the large-scale baroclinic zone in the Iceland area several small vortices start to grow. Eventually, one of these lows dominates at the expense of the others, and grows into a strong polar low. Shapiro, Fedor and Hempel (1987) observed strong surface winds (35 m s^{-1} at 300 m above the sea surface) and extremely strong vorticity ($18 \times f$). Surface pressure at the center of the low was 980 hPa.

5. Results

The role of released latent heat in a pure baroclinic process is to decrease the effective static stability in regions of ascent. This enhances the vertical vorticity and hence the vorticity by vortex stretching. Thus, release of latent heat may intensify baroclinic development, but it should be stressed that release of latent heat is not necessary for energy to be released by a baroclinic process. On the other hand, organized convection or CISK is driven by the release of latent heat. Without moisture supply organized convection cannot take place. Polar lows have been compared with tropical cyclones due to their strength, small horizontal scale, low central pressure, and possible driving mechanism (CISK). It is known that release of latent heat alone is insufficient to explain the extreme low surface pressure found in tropical cyclones. The crucial factor is the formation of an eye with subsidence in the center. In fact, 90% of all tropical disturbances fail to develop an eye and never reach hurricane intensity (Anthes, 1982). For a stable stratification, release of latent heat due to condensation in updraughts and vertical advection of potential temperature are counteracting processes. To obtain the strongest developments, condensation must organize so that ascending motion is surrounding an area of subsidence. Such distributions of upward and downward motion will increase horizontal temperature gradients which in turn enhance the vertical wind shear as seen from the thermal wind relation.

Thus the way latent heat is released may be important in explaining the initiation and growth of polar lows. By the experiments described in Table 1, the role of released latent heat in both baroclinic developments and in CISK-like developments may be studied. If baroclinicity is the most important driving mechanism, one should expect developments also in the DRY model. The NOC experiment will tell if this possible development is modified by latent heat release, or if large scale latent heat release is a crucial factor. If organized convection is the key in understanding the growth of the polar lows, one should look for subsidence in the center of the lows surrounded by strong convective activity. The role of cloudscale convection versus mesoscale convection is studied by the SLVC-runs.

5.1. *Reference experiment*

Some modellers (e.g., Orlanski and Ross, 1984) have suggested that explicit treatment of condensation processes is an alternative to convective parameterization for mesoscale models with horizontal resolution 50 km or less. This is an attractive approach since explicit condensation processes are simple to code and are efficient from a computational point of view. The NOC experiment is therefore taken as a reference experiment.

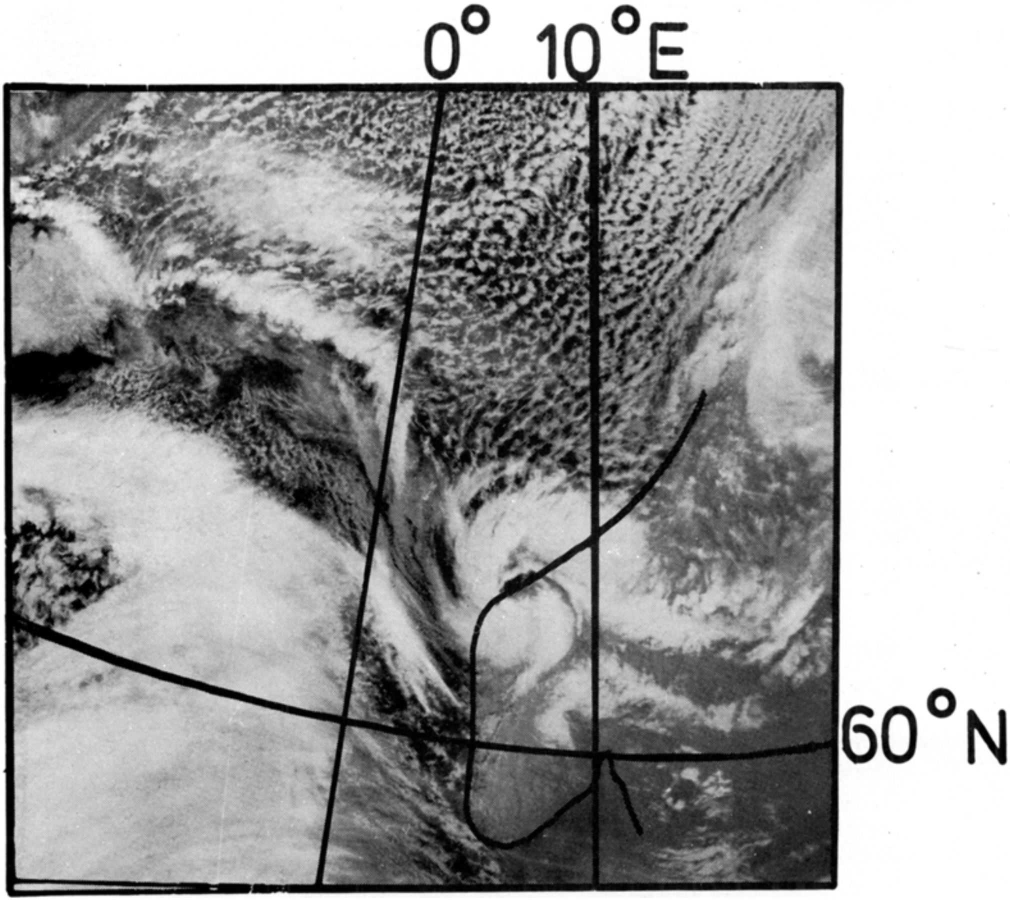

Fig. 5. Satellite picture from 14.45 GMT 1 March 1984 (corresponds to 26 hours 45 minutes of integration) showing the mature polar low off the coast of Norway.

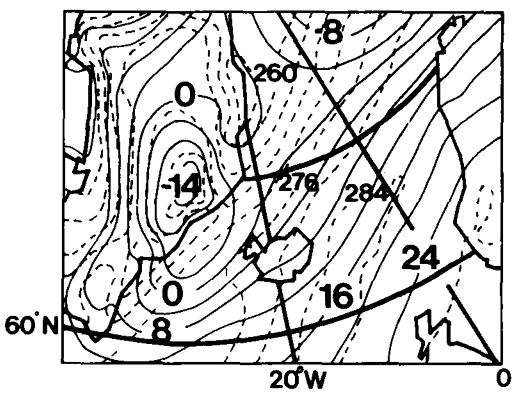

Fig. 6. Contours of 1000 hPa (solid lines, at intervals of 4 da m) and (potential) temperature at 1000 hPa (dashed lines, at intervals of 4 K) for 00.00 GMT 26 February 1984.

5.1.1. Boundary layer transition. As the arctic air for the 1 March case progresses towards the southwest it is heated from below by the warm sea surface. Fig. 7 shows cross sections along the line AA′ in Fig. 4. As seen, the height of the well mixed boundary layer increases as the air is heated from below. The boundary layer is capped by a strong inversion. A similar structure for cold air outbreak off the ice capped polar basin was observed by the NOAA Arctic Cyclone Experiment, (M. Shapiro, personal communication).

5.1.2. Frontal circulation. Fig. 8a shows the term, $J_{xp}(U, V) = U_x V_p - V_x U_p$, which is proportional to the geostrophic forcing, after 6 hours of integration with the DRY model. The cross section is taken along line BB′ in Fig. 4. U and V are geostrophic wind components perpendicular to and along the front respectively. At this time

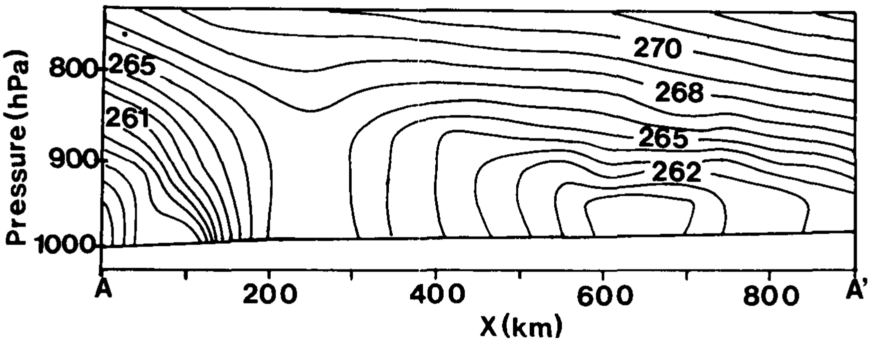

Fig. 7. Vertical cross section (72.4°N, 14.6°W) to (73.2°N, 27.6°E) after 6 hours of integration with NOC starting from 12.00 GMT 29 February 1984 showing potential temperature at intervals of 1 K. Position of cross section is shown in Fig. 4.

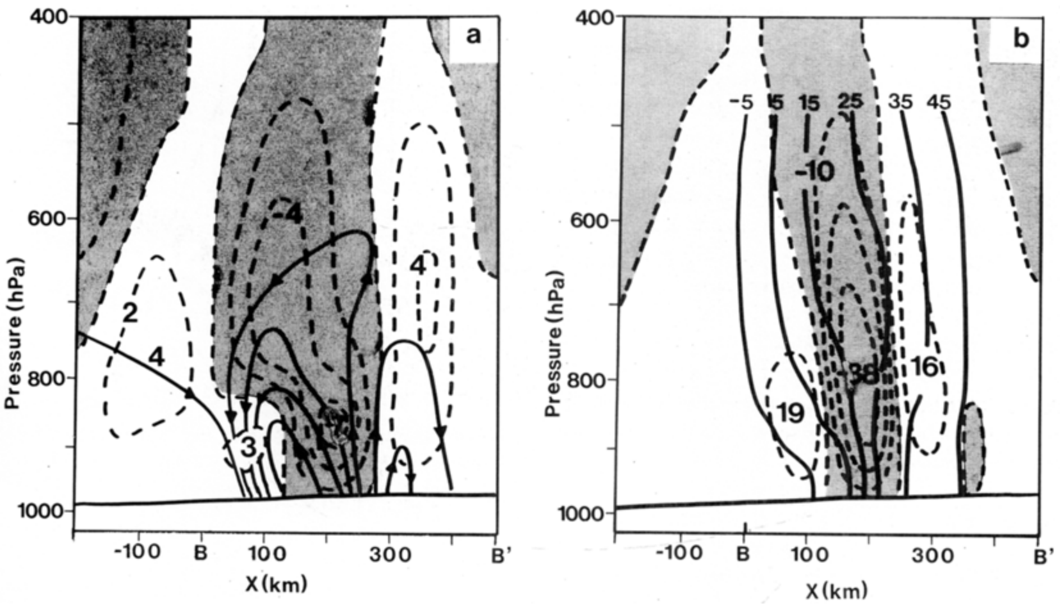

Fig. 8. Vertical cross section (64.2°N, 0.2°E) to (69.0°N, 9.3°E) after 6 hours of integration from 12.00 GMT 29 February 1984. (a) Model DRY. Dashed lines are contours of vertical velocity, ω, at intervals of 1×10^{-3} hPa s^{-1}. Solid lines are contours of geostrophic forcing $J_{xp}(U, V)$. See text. Arrows on geostrophic forcing contours indicate direction of circulation. (b) Model NOC. Dashed lines are contours of vertical velocity, ω, at intervals of 10×10^{-3} hPa s^{-1}. Solid lines are contours of absolute momentum at intervals of 10 m s^{-1}. Shading denotes areas of ascending motion. Position of cross section is shown in Fig. 4 (BB').

the line is approximately perpendicular to the front. There is geostrophic deformation at both sides of the warm air (shear deformation at the leading front and confluence at the weaker rear front). The vertical velocity field (Fig. 8a) is in accordance with the theory of ageostrophic circulation in frontal zones as described by Eliassen (1962). Due to the definition of the x-axis, positive values of $J_{xp}(U, V)$ leads to a circulation in the clockwise sense (viewed from the positive y-axis, i.e., viewed towards the reader), while negative forcing produces a circulation in the opposite direction. The circulation has a slope corresponding to the slope of the absolute momentum surfaces. Vertical velocity and some lines of constant absolute momentum are shown in Fig. 8b for the NOC integration. One notices that the vertical velocity in NOC is considerably stronger than in DRY, and that the circulation no longer tilts. A close examination reveals that the model atmosphere is actually absolutely unstable both with regard to vertical as well as slantwise convection. Thorpe and Nash (1984) studied vertical convection in frontal zones and showed that convective heating in the warm air disrupted the geostrophically forced (and stable) circulation. Here, the situation is even more complex, since there are geostrophic forcing together with a symmetric unstable stratification. The very strong vertical velocity (~ 30 cm s^{-1}) is probably the response of the hydrostatic governing equations to a kind of motion they are not designed to describe. Fig. 9 shows the temperature sounding at the operational weather ship M (65.6°N, 2.5°E) 00.00 GMT 1 March 1984 (12 hours of integration) and two model simulations. The model stratification is too unstable. This has a positive feedback on the vertical velocity and hence vorticity as discussed above, but is not necessarily physically correct. Figs. 10a, b show surface winds after 24 and 27 hours of integration from a section off the Norwegian coast. One notices the very strong winds and the closed circulation (black dot) in the same area as the polar low was observed.

The transition from three small disturbances to one deep polar low for the 27 February case is described in detail in Grønås et al. (1987) and will not be repeated here. The general performance of the model for this case is illuminated by plots of 1000 hPa heights after 24 and 39 hours of integration with NOC, valid at 00.00 GMT and 15.00 GMT 27 February 1984 (Fig. 11). The position and timing of the low (marked with a capital L) is forecasted approximately correctly. The intensity is, however, too weak. Shapiro et al. (1987) observed a central pressure value of 980 hPa.

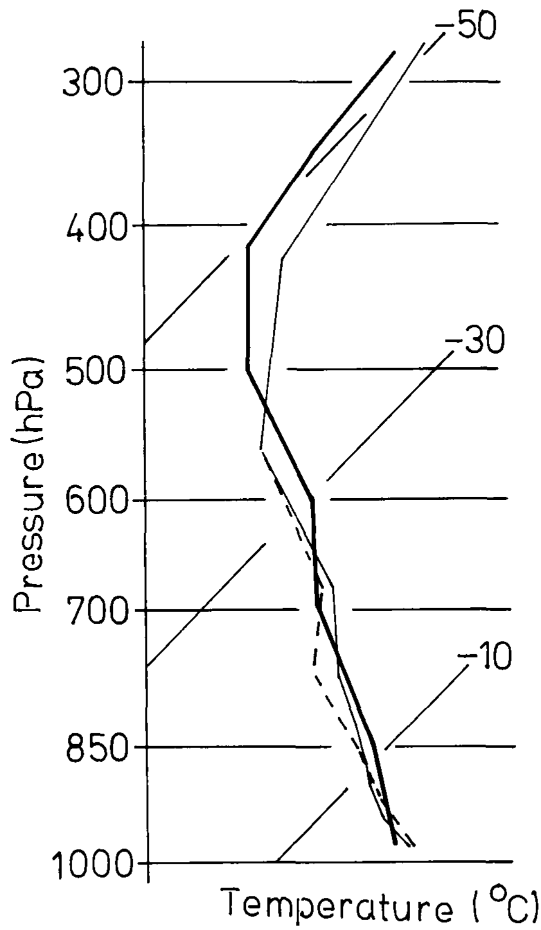

Fig. 9. Temperature sounding at the operational weather ship M (65.5°N, 2.5°E) 1 March 1984 00.00 GMT (thick line) and 12 hour forecasts from 12.00 GMT 29 February 1984 with models NOC (dashed line) and model SLVC2 (solid thin line).

5.2. *The impact of condensation*

When moist processes are excluded (experiment DRY) the model still adjusts to the high resolution giving detailed flow fields, but the final growth of the polar lows is either missing or significantly weaker compared to simulations with condensation. Fig. 10c shows winds at $\sigma = 0.975$ off the western coast of Norway after 27 hours of integration with model DRY for the 1 March case. The position of the front is correctly simulated but winds are weak and no closed circulation is indicated. Fig. 10c should be compared to Fig. 10d and Fig. 10e from the VC and SLVC2 runs.

For the 27 February case, a low is forecasted at approximately the correct position and time with the DRY-model (not shown), though it is some-

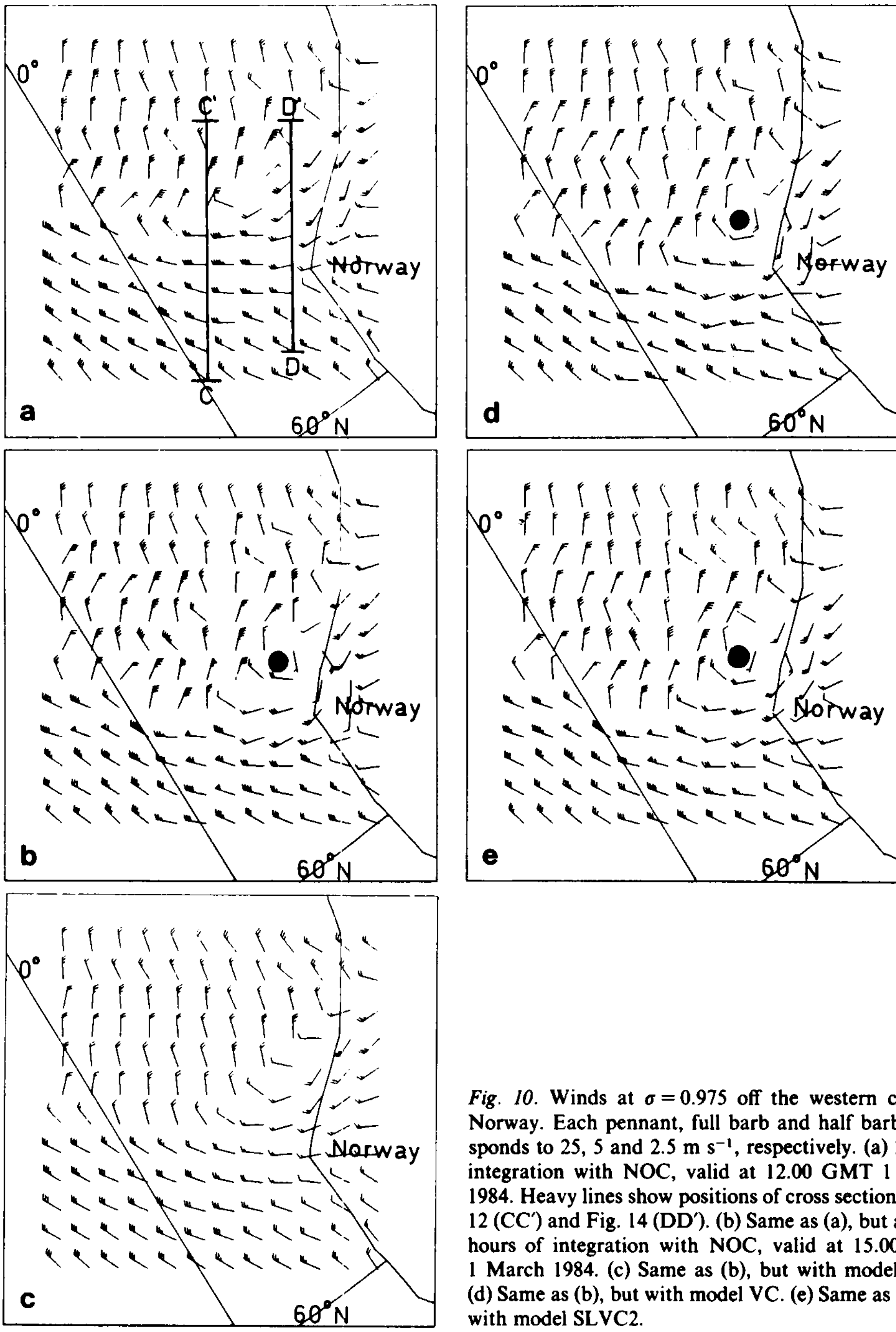

Fig. 10. Winds at $\sigma = 0.975$ off the western coast of Norway. Each pennant, full barb and half barb corresponds to 25, 5 and 2.5 m s^{-1}, respectively. (a) 24-hour integration with NOC, valid at 12.00 GMT 1 March 1984. Heavy lines show positions of cross section in Fig. 12 (CC′) and Fig. 14 (DD′). (b) Same as (a), but after 27 hours of integration with NOC, valid at 15.00 GMT 1 March 1984. (c) Same as (b), but with model DRY. (d) Same as (b), but with model VC. (e) Same as (b), but with model SLVC2.

what weaker than in the moist experiments (-16 m versus -43 m for NOC). A closer examination reveals, however, that the low has evolved somewhat differently as compared to moist experiments. The growing low in the DRY experiment is the eastward moving lee cyclone found between Iceland and Greenland 00.00 GMT 27 March 1984 (Fig. 11a). The low marked "L" in Fig. 11a is not developing in the DRY experiment.

5.3. The impact of deep convection (cloud-scale condensation)

The overall effect of deep convection (VC) compared to grid resolvable condensation (NOC) is to release latent heat at high levels and to stabilize the atmosphere. Sardie and Warner (1985) showed that parameterization of convection was necessary to prevent over-development for one of their test cases. Here, it is found that the model atmosphere stabilizes when convection is parameterized. The unstable region at weather ship M found in the NOC-run (Fig. 9) has disappeared. It may also be seen from cross sections along line CC′ in Fig. 10a. Fig. 12 shows that the decrease with height of equivalent potential temperature is significantly reduced in VC (Fig. 12b) as compared to NOC (Fig. 12a).

In the early stages of the integration, there are small differences between vertical velocity from VC and NOC (Fig. 8 shows results from NOC). A possible explanation is that CAPE is large at low levels in the beginning of the integration, so that the air is heated mainly at these levels. The overall effect would be nearly the same as for explicit condensation. After 24 hours of integration NOC still shows strong vertical velocity related to an unstable stratification (Fig. 13a). Parameterization of convection (Fig. 13b) is seen to suppress the ascending motion while the descending motion is enhanced. The large scale response to parameterized convection is therefore to create descending motion close to the area of parameterized heating. From Fig. 13b one would expect strong low level convergence at the center of the disturbance.

Several cross-sections have been scrutinized through the frontal zone for the 1 March case. Almost all have ascending motion in connection with the leading front but also right above the surface disturbance. Fig. 13b is an example. Exceptions are found in cross-sections through the circulation center after 27 hours of integration (corresponds to 15.00 GMT 1 March 1984) for the simulations with convection. A nice example of subsidence in the center of the low, "the eye", is found in the VC-run (Fig. 14). The section is along the line DD′ in Fig. 10a. One must, however, be careful not to draw too strong conclusions from looking at instantaneous plots of vertical velocity which may fluctuate due to noise. Mean vertical velocity over some time is reflected, however, in the precipitation pattern. The area of no precipitation (Fig. 15), which should be compared with the cloudfree area on the satellite picture of Fig. 5, indicates that the

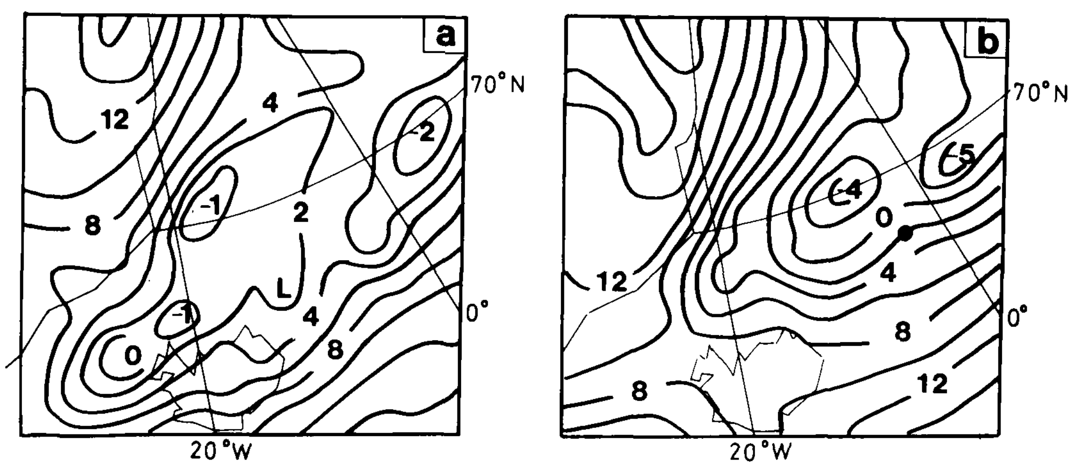

Fig. 11. Contours of 1000 hPa at intervals of 2 da m. Integration with NOC from 00.00 GMT 26 February 1984. (a) 24-hour integration. The trough marked with a capital L is the growing polar low. (b) 39-hour integration. The black dot is the observed position of the polar low.

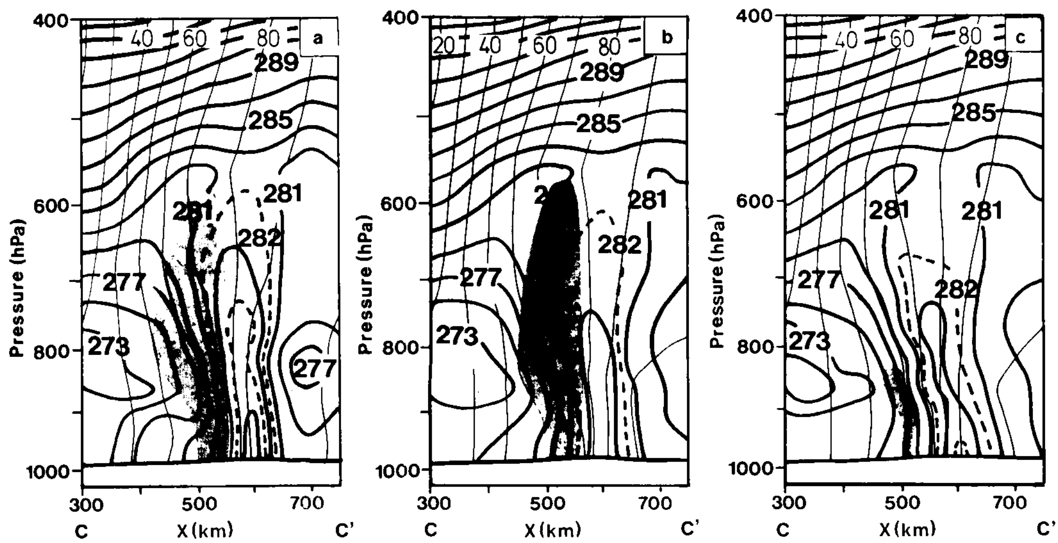

Fig. 12. Vertical cross section (61.5° N, 0.1° E) to (64.9° N, 5.3° E) after 24 hours of integration, valid at 12.00 GMT 1 March 1984. Thick lines are contours of equivalent potential temperature at intervals of 2 K and 1 K (dashed lines). Thin lines are contours of absolute momentum at intervals of 10 m s^{-1}. (a) Model NOC. (b) Model VC. (c) Model SLVC2. Shading denotes areas of symmetric instability. Position of cross section is shown in Fig. 10a (CC′).

subsidence has lasted for at least three hours. However, the possible organized convection is either too brief or too weak, possibly due to poor resolution. It does not manifest in a strong drop in surface pressure. Similar patterns are found in both SLVC-runs but are not as clear in NOC, which has a precipitation minimum in the same area.

Also for the 27 February case, plots of vertical velocity suggest that some kind of organized convection has been initiated. Center subsidence is found in the mature stage of the low (not shown). During its growing phase, only small amounts of convective precipitation is recorded suggesting that parameterization of convection has minor impacts on the simulation of this polar low. The low becomes slightly deeper when vertical convection is parameterized (−53 m for VC and −43 m for NOC), but the difference is small.

5.4. *The impact of slantwise convection (mesoscale condensation)*

Inclusion of slantwise convection has a clear impact on the 1 March case, but its influence is not as clear on the 27 February case. This section will therefore concentrate on the 1 March case.

Equivalent potential temperature and absolute momentum from NOC, VC and SLVC2 along line CC′ in Fig. 10a reveal that the structure of fronts is changed when slantwise convection is parameterized (Fig. 12). The region of maximum equivalent potential temperature has a tilt corresponding to the tilt of the front in the SLVC2-run, thus enhancing the vertical instability right above and behind the surface disturbance while stabilizing it in front of the disturbance. The tilt of the axis of maximum equivalent potential temperature is also found in SLVC1 (not shown), but not as clear as in SLVC2. NOC and VC are seen to be potentially unstable to slantwise convection along the leading front. In contrast, SLVC2 is nearly perfectly neutral to symmetric overturnings. The tilt of the area of maximum equivalent potential temperature is caused by heating and moistening in the upper regions of the front due to parameterized slantwise convection. At this stage of the front development, there is no clear geostrophic forcing. One would, however, expect convective

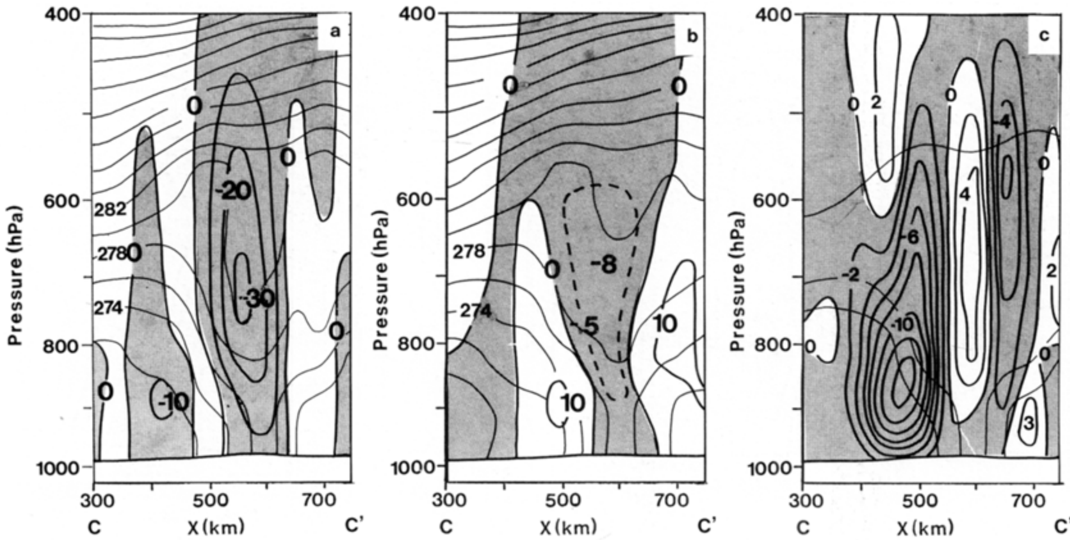

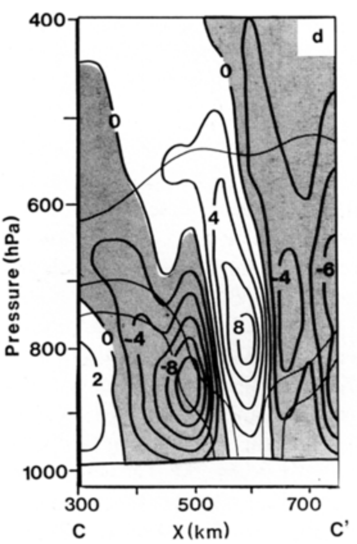

Fig. 13. Same cross section as in Fig. 12. (a) Model NOC. Thick lines are contours of vertical velocity, ω, at intervals of 10×10^{-3} hPa s^{-1}, thin lines are contours of potential temperature at intervals of 2 K. (b) As in (a), but model VC. Thick dashed line is contour of $\omega = -5 \times 10^{-3}$ hPa s^{-1}. (c) Thick lines are contours of differences in vertical velocity between SLVC1 and VC at intervals of 2×10^{-3} hPa s^{-1}. Thin lines are contours of the potential temperature surfaces 274 K, 278 K and 280 K, respectively. (d) As (c), but the difference between SLVC2 and VC. Shading denotes areas of ascending motion. Position of section is shown in Fig. 10a (CC′).

activity along the sloping front due to the unstable stratification. NOC and VC show no signs of such a motion. In fact, strong descent is found at the front in the VC experiment (Fig. 13b). When slantwise convection is parameterized, the area of ascending motion is extended towards the colder air. This manifests clearly in differences in vertical velocity between the SLVC-runs and VC (Figs. 13c and d), showing a thermally indirect circulation consistent with the response to a point source of diabatic heating (Eliassen, 1959). Eliassen showed that a central updraught is expected through the source region with slope along the absolute momentum surfaces. The return flow is provided by elliptic cells on either side. Strictly speaking, the theory applies only to stable circulations, but the similarity is astonishing. This result is in agreement with Thorpe (1984), who found a thermal indirect return flow with descent in the warm air when sloping convection were parameterized in a forced circulation. The main picture is the same for SLVC1 and SLVC2

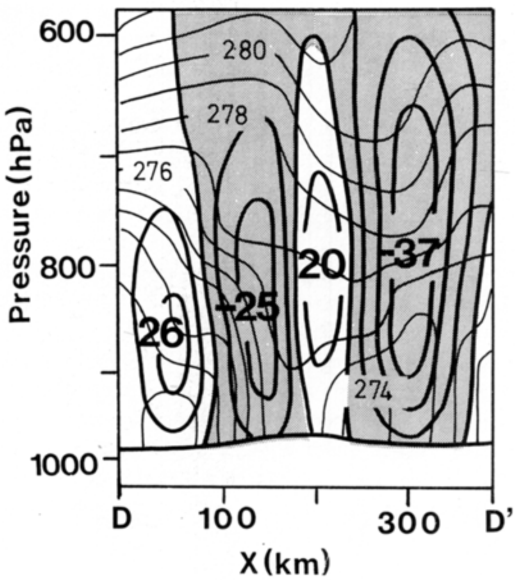

Fig. 14. Vertical cross section (61.4°N, 2.2°E) to (64.3°N, 7.0°E) after 27 hours of integration with model VC from 12.00 GMT 29 February 1984. Valid at 15.00 GMT 1 March 1984. Thick lines are contours of vertical velocity, ω, at intervals of 10×10^{-3} hPa s^{-1}. Thin lines are contours of potential temperature at intervals of 1 K. Shading denotes areas of ascending motion. Position of cross section is shown in Fig. 10a (DD′).

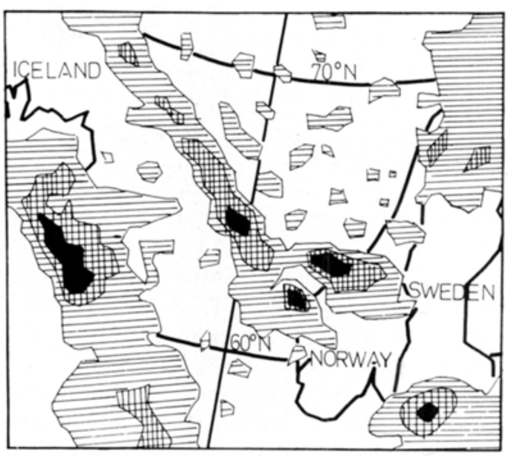

Fig. 15. Large scale and vertical convective precipitation exceeding 0.1 mm/3 hour accumulated between 24 and 27 hours of integration in the VC-run. Doubled hatched areas correspond to precipitation exceeding 1 mm/3 hour, black areas for precipitation greater than 1 mm/hour.

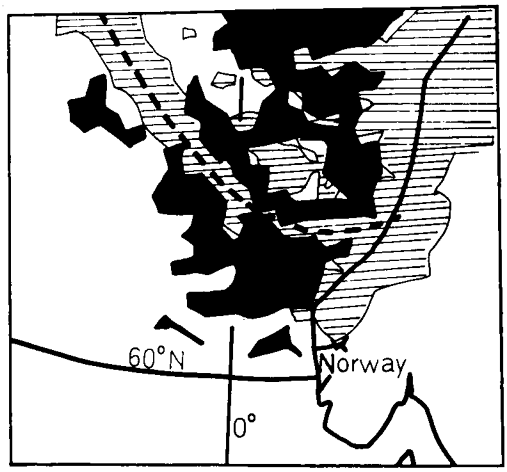

Fig. 16. A composite picture of accumulated large-scale and vertical convective precipitation (hatched) and slantwise convective precipitation exceeding 0.1 mm/3 hour (black) between 18 and 21 hours of integration for the case of 1 March 1984. The leading surface front after 21 hours of integration is shown as a dashed line.

though there are significant differences. The induced circulation has no tilt in the SLVC1 parameterization. The descending motion in the warm air is weaker and have maximum at higher levels as compared to SLVC2. From these figures one would expect that the low level frontogenesis is stronger in the SLVC-runs than in VC.

Precipitation from slantwise convection aligns in bands parallel to the front and there is a tendency for the bands to be found in complementary areas compared to large-scale and vertical convective precipitation (Fig. 16).

Parameterization of turbulent momentum transport (friction) is the same for all experiments including DRY. However, other physical processes (e.g., condensation) of course influence horizontal velocities indirectly by a rearrangement of the temperature distribution followed by geostrophic adjustment. For the 1 March experiment, all moist experiments lead to enhanced surface winds as compared to DRY. Conservation of absolute momentum is automatically taken care of in SLVC2, and there is an indication of a small but significant wind enhancement in the northeasterly flow behind and the northwesterly jet ahead of the front in SLVC2. This manifests in a slightly larger vorticity. At the position of the polar low (black dot), however, the vorticity is slightly larger in VC. Not surprisingly, the strongest winds are obtained from NOC.

Parameterization of slantwise convection seems to have small impacts on the simulation of the polar low from the case of 27 February 1984. Potential vorticity is slightly negative in the cold air to the south. However, small amounts of precipitation from slantwise convection are recorded (indicating minor heating from slantwise convection), and the final depth of the low is practically the same as in VC (~ -53 m). This case was also run with high vertical resolution in the Planetary Boundary Layer to see if the vertical resolution has a significant effect on whether slantwise and vertical convection are initiated or not. The results are qualitatively the same as when coarse vertical resolution is used. The low becomes, however, slightly deeper, (-76 m versus -53 m with coarse vertical resolution).

During each forecast the horizontal distance from the grid-point under consideration to the point where the M-surface intersects with a surface of constant pressure is recorded. A mean value for the whole integration domain varies between one and two gridlengths with a standard deviation close to one fifth of a gridlength.

6. Discussion

Condensation schemes for different scales have been applied on two polar low cases over the Norwegian Sea. The model simulates successfully vortices at the right position and time in all experiments. Condensation is, however, crucial in order to obtain sufficiently strong polar lows.

The two cases studied here, suggest that release of latent heat is the most important factor in the strong and fast growth of polar lows. However, vertical and horizontal distribution of heating are also important. Convection shifts the area of maximum heating upwards, while slantwise convection in addition spreads the heating horizontally away from the surface disturbance.

We have found that the model atmosphere becomes too unstable when condensation is treated explicitly (i.e., precipitation occurs only after saturation is reached on the grid scale). If one is concerned about how well the model simulates the surface depression of the polar lows, there are no *major* improvements when convection (slantwise as well as vertical) is parameterized, but the model atmosphere responses to the parameterized convection in a physically sound way. These results therefore support the study of Molinari and Corsetti (1985) who found that convection had to be parameterized to simulate a mesoconvective system (MCC) over the United States. The conclusion of Orlanski and Ross (1984) in that an explicit treatment of convection is sufficient for models with resolution 50 km or less was not supported by Molinari and Corsetti (1985), and is not supported by this study either.

Most parameterization schemes concentrate on scales which have a large separation from the grid size. The horizontal scales on which the scheme for slantwise convection operates are of the same order as the gridlength (50–100 km), and there is no clear separation between the phenomenon we want to parameterize and the grid scale. However, motion on the grid length scale should be damped to avoid aliasing, and we claim that motion on scales too small to be adequately resolved by the model grid should be parameterized. The results shown by cross sections through a frontal zone for one of our test cases supports this idea.

Here it is found that low level winds become slightly stronger when slantwise convection is working. This might come from the fact that more moisture is condensed (the scheme works when conditions for upright convection are not fulfilled), or is due to the horizontal distribution of heating. Since local high pressure with outflow will develop above a heated region, the idea of spreading the heating upwards and away from the surface disturbance is appealing. A configuration with convergence in the upper regions above the surface low and subsidence in the center is then possible. This is not the case if convection takes place right above the surface disturbance.

For one of the test cases, nice improvements are found when slantwise convection is parameterized in addition to vertical convection. The model adjusts to a state less unstable to symmetric instability and shifts areas of ascending motion towards the frontal zones. The difference in vertical velocity between experiments where slantwise convection is parameterized in addition to vertical convection and when only vertical convection is parameterized, indicates that heating from parameterized slantwise convection initiates a secondary circulation, consistent with a point source of heating as described by Eliassen (1959).

However, slantwise convection does not play the key-role in these simulations. A natural extension of this work is therefore to see the effect of refinements within the scheme for slantwise convection. In particular, sensitivity to different closure methods for both vertical and slantwise convection should be investigated. The method which is used here to determine moisture supply for convection is simple, but it at least reflects that convection very well may be triggered independently of large scale moisture convergence. A closure assumption worth trying is to activate the scheme for slantwise convection not only for conditionally unstable stratifications along the absolute momentum surfaces (as here), but also for potentially unstable stratifications if the geostrophic forcing is strong enough to raise the air parcel to the level of free convection. In this study, the model sounding is first checked for vertical instability. This is *a priori* correct since the most unstable direction is upright, when conditions for vertical convection and slantwise convection both are present (Emanuel, 1983b). The scheme for slantwise convection is approximately consistent with regard to conservation of angular momentum, while schemes for vertical convection are not. Assume that a vertically lifted air parcel conserves its angular momentum. After reaching its level of *vertical* equilibrium, it will have a different angular momentum than the surroundings, and either dissolve giving away its extra momentum to the environments, or start a horizontal drift towards its absolute equilibrium position. This equilibrium position is actually on the absolute momentum surface from the level where the parcel started its buoyant ascent. A more consistent way to perform convective parameterization may therefore be to lift air parcels directly along surfaces of constant absolute momentum whether or not the atmosphere is unstable to vertical convection. Further research will continue along the lines mapped out here. Such experiments may easily be performed within the frame of parameterization of slantwise convection described in this paper.

In any case, when the atmosphere becomes unstable to symmetric perturbations, one should expect symmetric overturnings in the most unstable direction. To simulate the atmosphere as correctly as possible, such an instability release should be taken into account in numerical models. The parameterization scheme for slantwise convection described here takes care of and adjusts symmetrically unstable regions towards a neutral condition. The length scale of slantwise convection is of the same order as the grid scale, showing that even for a grid point model with a resolution of 50 km, a parameterization technique is necessary.

It is impossible to draw a general conclusion about the driving mechanism of polar lows from two cases, especially as different mechanisms seems to be working separately or in combinations with each other. Concerning the cases studied here, the experiments indicate that "dry-processes" (e.g., deformation and baroclinicity) transform the atmosphere to a state which is favourable for organized convective motion. This organized convection may in turn take over as the main driving mechanism of the disturbance. The model seems to have a potential for creating subsidence in the centre of the lows, but the subsidence is not manifesting in a significant pressure drop. It is possible that the scale of the lows is too small for a proper simulation with a grid-point model with resolution 50 km.

7. Acknowledgement

The author would like to thank colleagues at the Norwegian Meteorological Institute and Melvin Shapiro, NOAA/WPL, Boulder, Colorado, USA for comments and valuable discussions in our attempts to understand the physics behind the polar lows. Kerry Emanuel, MIT, gave inspiration and had useful ideas regarding momentum transport and other aspects of the scheme for slantwise convection. Anstein Foss, Sigbjørn Grønås and Magne Lystad are thanked for providing the mesoscale model and data for the experiments. Anstein Foss was an inestimable consultant regarding the numerical set-up of the experiments. The work has been performed while the author was engaged as a Norwegian representative in the HIRLAM project (High Resolution Limited Area Model) financed by the Nordic Council and participating countries.

8. Appendix

Emanuel (1983b) defines Slantwise Convective Available Potential Energy (SCAPE) as the positive area on a tephigram obtained when a parcel is lifted along a surface of constant absolute momentum M, and the potential temperature of the parcel θ_p is compared to that of the environments θ_g.

$$\mathrm{SCAPE} = \int_1^2 (\theta_p - \theta_g)_M \, d\pi. \tag{A.1}$$

SCAPE can be estimated from:

$$\mathrm{SCAPE} = \mathrm{CAPE} + \int_{z_0}^{z_1} \frac{f}{2\eta} \frac{d}{dz}((v - v_0)^2)\, dz, \tag{A.2}$$

where CAPE is the usual area measured for vertical lifting on a tephigram (area between actual sounding and the moist abiabat from the lifting level). The last term is the contribution from the thermal wind, which may be large enough to compensate for significant negative values of CAPE if the windshear is large. Emanuel (1983b) developed this equation by assuming geostrophic wind, conservation of potential temperature and that the thermal wind is not a function of the horizontal distance along the absolute momentum surface. Assuming vanishing moist potential vorticity, one gets:

$$\frac{\partial \theta_e}{\partial p} = \eta^{-1} \boldsymbol{k} \cdot \nabla \theta_e \times \frac{\partial \boldsymbol{v}}{\partial p}. \tag{A.3}$$

In a saturated atmosphere, the thermal wind equation may approximately be written as:

$$f\, \partial \boldsymbol{v}_g / \partial z = g\gamma \boldsymbol{k} \times \nabla \ln \theta_e, \tag{A.4}$$

where γ is the ratio between the moist adiabatic and the dry adiabatic lapse rates

$(T_z(\text{moist ad.})/T_z(\text{dry ad.}))$

and $\boldsymbol{v}_g$ is the geostrophic wind (Emanuel, 1983a). Introducing $(\partial/\partial z = -g\theta^{-1}\, \partial/\partial \pi)$ gives,

$$\nabla \theta_e = \frac{f\theta_e}{\gamma\theta} \boldsymbol{k} \times \frac{\partial \boldsymbol{v}_g}{\partial \pi}. \tag{A.5}$$

It is further assumed that the wind is geostrophic.

By introducing (A.5) into (A.3), one obtains:

$$\frac{\theta}{\theta_e} \frac{\partial \theta_e}{\partial \pi} = -\frac{f}{\eta\lambda} \left(\frac{\partial \boldsymbol{v}}{\partial \pi} \right)^2, \tag{A.6}$$

where λ is equal to one when condensation is not taking place and is given by γ for a saturated atmosphere. (A.6) shows that for a given windshear equivalent potential temperature must increase with height in order to have a non-negative potential vorticity. Writing

$(\theta/\theta_e)(\partial \theta_e/\partial \pi) = \theta(\partial \ln \theta_e/\partial \ln \theta)(\partial \ln \theta/\partial \pi)$

and observing that $(\partial \ln \theta_e/\partial \ln \theta) = \gamma^{-1}$, then integration from an arbitrary level π to level π_0, which for instance may represent the cloud base, gives,

$$\theta(\pi_0) - \theta(\pi) = -\int_{\pi}^{\pi_0} \frac{f}{\eta} \left(\frac{\partial \boldsymbol{v}}{\partial \pi} \right)^2 d\pi. \tag{A.7}$$

$\theta(\pi_0)$ is the potential temperature representing the moist adiabat from π_0, while $\theta(\pi)$ is the potential temperature required for vanishing potential vorticity. SCAPE is defined as the positive area on a tephigram when the temperature of the reversibly lifted parcel (θ_p) from π_0 (base) to π_1 (top) is compared to the temperature of the environments (θ_g).

$$\mathrm{SCAPE} = \int_{\pi_1}^{\pi_0} \theta_p - \theta_g \, d\pi$$
$$= \int_{\pi_1}^{\pi_0} \theta_p - \theta_0 \, d\pi + \int_{\pi_1}^{\pi_0} \theta_0 - \theta_g \, d\pi. \tag{A.8}$$

Here the second integral to the right is seen to be the area between the moist adiabat from π_0 and the environments. This area is usually called Convective Available Potential Energy (CAPE). By introducing from (A.9), one ends up with,

$$\mathrm{SCAPE} = \mathrm{CAPE} + \int_{\pi_1}^{\pi_0} \int_{\pi}^{\pi_0} \frac{f}{\eta} \left(\frac{\partial \boldsymbol{v}}{\partial \pi} \right)^2 d\pi \, d\pi. \tag{A.9}$$

Assuming f/η to be constant (or to represent a mean value within π_1 and π_0) and performing the integration give:

$$\mathrm{SCAPE} = \mathrm{CAPE} + \frac{f}{2\eta} (\boldsymbol{v}_1 - \boldsymbol{v}_0)^2, \tag{A.10}$$

which corresponds to eq. (17) in Emanuel (1983b).

REFERENCES

Anthes, R. A. 1977. Hurricane model experiments with a new cumulus parameterization scheme. *Mon. Wea. Rev. 105*, 287–300.

Anthes, R. A. 1982. Tropical cyclones. Their evolution, structure and effects. *Meteorol. Monogr. 19*, American Meteorological Society.

Bennets, D. A. and Hoskins, B. J. 1979. Conditional symmetric instability—a possible explanation for frontal rainbands. *Q. J. R. Meteorol. Soc. 105*, 945–962.

Bratseth, A. 1985. A note on CISK in polar air masses. *Tellus 37A*, 403–406.

Charney, J. G. 1962. Integration of the primitive and balance equations. Proc. Symp. Numerical Weather prediction, Tokyo, 131–152.

Eliassen, A. 1959. On the formation of fronts in the atmosphere. In *The atmosphere and the sea in motion.* N.Y. Rockefeller Institute Press, 277–287.

Eliassen, A. 1962. On the vertical circulation in frontal zones. *Geofys. Publ. 24*, 147–160.

Emanuel, K. A. 1982. Inertial instability and mesoscale convective systems. Part II: Symmetric CISK in a baroclinic flow. *J. Atmos. Sci. 39*, 1080–1096.

Emanuel, K. A. 1983a. The lagrangian parcel dynamics of moist symmetric instability. *J. Atmos. Sci. 40*, 2368–2376.

Emanuel, K. A. 1983b. On assessing local conditional symmetric instability from atmospheric soundings. *Mon. Wea. Rev. 111*, 2016–2033.

Emanuel, K. A. 1985. Frontal circulations in the presence of small moist symmetric stability. *J. Atmos. Sci. 42*, 1062–1071.

Grønås, S. and Hellevik, O. E. 1982. A limited area prediction model at the Norwegian Meteorological Institute. Techn. Rep. No. 61, Det Norske Meteorologiske Institutt, Oslo, Norway.

Grønås, S., Foss, A. and Lystad, M. 1987. Numerical simulations of polar lows in the Norwegian Sea. *Tellus 39A*, 334–353.

Harrold, T. W. and Browning, K. A. 1969. The polar low as a baroclinic disturbance. *Q. J. R. Meteorol. Soc. 95*, 710–723.

Iversen, T. and Nordeng, T. E. 1984. A hierarchy of nonlinear filtered models—numerical solutions. *Mon. Wea. Rev. 112*, 2048–2059.

Krishnamurti, T. N., Kanamitsu, M., Godbole, R., Chang, C. B., Carr, F. and Chow, J. 1976. Study of a monsoon depression (II). Dynamical structure. *J. Meteorol. Soc. Japan 54*, 208–225.

Kuo, H. L. 1965. On formation and intensification of tropical cyclones through latent heat release by cumulus convection. *J. Atmos. Sci. 22*, 40–63.

Kuo, H. L. 1974. Further studies of the parameterization of the influence of cumulus convection on large scale flow. *J. Atmos. Sci. 31*, 1232–1240.

Kuo, Y.-H. and Anthes, R. A. 1984. Semiprognostic tests of Kuo-type cumulus parameterization schemes in an extratropical convective system. *Mon. Wea. Rev. 112*, 1498–1509.

Louis, J. F. 1979. A parametric model of vertical eddy fluxes in the atmosphere. *Boundary Layer Meteorol. 17*, 187–202.

Molinari, J. and Corsetti, T. 1985. Incorporation of cloud-scale and mesoscale downdraughts into a cumulus parameterization: Results of one- and three-dimensional integrations. *Mon. Wea. Rev. 113*, 485–501.

Økland, H. 1977. On the intensification of small-scale cyclones formed in very cold air masses heated by the ocean. Institute report series. Department of Geophysics, University of Oslo, Norway.

Orlanski, I. and Ross, B. B. 1984. The evolution of an observed cold front. Part II: Mesoscale dynamics. *J. Atmos. Sci. 41*, 1669–1703.

Rasmussen, E. 1981. An investigation of a polar low with a spiral cloud structure. *J. Atmos. Sci. 38*, 1785–1792.

Reed, R. J. 1979. Cyclogenesis in polar air streams. *Mon. Wea. Rev. 107*, 38–52.

Sardie, J. M. and Warner, T. T. 1983. On the mechanism for the development of polar lows. *J. Atmos. Sci. 40*, 869–881.

Sardie, J. M. and Warner, T. T. 1985. A numerical study of the development mechanism of polar lows. *Tellus 37A*, 460–477.

Seltzer, M. A., Passarelli, R. E. and Emanuel, K. A. 1985. The possible role of symmetric instability in the formation of precipitation bands. *J. Atmos. Sci. 42*, 2207–2219.

Shapiro, M. A., Fedor, L. S. and Hampel, T. 1987. Research aircraft measurements of a polar low over the Norwegian Sea. *Tellus 39A*, 272–306.

Thorpe, A. 1984. CISK as a basis for convective parameterization in baroclinic flows—application to frontal developments. Proceedings. Convection in large-scale numerical models. ECMWF, Shinfield Park, Reading, UK, 139–169.

Thorpe, A. 1986. Parameterization of mesoscale processes. Proceedings. Seminar on Physical Parameterization for Numerical Models of the Atmosphere. ECMWF, Shinfield Park, Reading, UK, 205–233.

Thorpe, A. J. and Nash, C. A. 1984. Convective and boundary layer parameterization in a diagnostic model of atmospheric fronts. *Q. J. R. Meteorol. Soc. 110*, 443–466.

Thorpe, A. J. and Emanuel, K. A. 1985. Frontogenesis in the presence of small stability to slantwise convection. *J. Atmos. Sci. 42*, 1809–1824.

Wilhelmsen, K. 1985. Climatological study of gale-producing polar lows near Norway. *Tellus 37A*, 451–459.